ACS Catalysis
Research Article
pubs.acs.org/acscatalysis

Catalysis on Singly Dispersed Rh Atoms Anchored on an Inert Support

Shiran Zhang,[†,&] Yan Tang,[‡,&] Luan Nguyen,[†] Ya-Fan Zhao,[‡] Zili Wu,[§] Tian-Wei Goh,[∥] Jimmy Jingyue Liu,[⊥] Yuanyuan Li,[#] Tong Zhu,[†] Wenyu Huang,[∥] Anatoly I. Frenkel,[#] Jun Li,*[,‡] and Franklin Feng Tao*[,†]

[†]Department of Chemical and Petroleum Engineering and Department of Chemistry, University of Kansas, Lawrence, Kansas 66047, United States

[‡]Department of Chemistry and Key Laboratory of Organic Optoelectronics & Molecular Engineering of Ministry of Education, Tsinghua University, Beijing 100084, People's Republic of China

[§]Center for Nanophase Materials Sciences and Chemical Science Division, Oak Ridge National Laboratory, Oak Ridge, Tennessee 37831, United States

[∥]Department of Chemistry, Iowa State University, Ames, Iowa 50011, United States

[⊥]Department of Physics, Arizona State University, Tempe, Arizona 85287, United States

[#]Department of Physics, Yeshiva University, New York, New York 10016, United States

ABSTRACT: A metal catalyst supported on an inert substrate could consist of both metal nanoparticles and singly dispersed metal atoms. Whether these singly dispersed metal atoms are active and how different their catalytic mechanism could be in contrast to a supported metal catalyst are fundamentally important for understanding catalysis on a supported metal or oxide. By taking reduction of NO with CO on singly dispersed Rh atoms anchored on an inert support SiO_2 as a probe system (Rh_1/SiO_2), here we demonstrated how *singly dispersed* metal atoms on an inert support could perform a complex multi-step catalytic cycle through a mechanism distinctly different from that for a supported metal nanoparticle with *continuously packed* metal sites. These singly dispersed Rh_1 atoms anchored on SiO_2 are active in reducing nitric oxide with carbon monoxide through two reaction pathways that are different from those of Rh nanoparticles. In situ IR studies show that a CO molecule and a NO molecule coadsorb on a singly dispersed Rh atom, Rh_1 anchored on SiO_2, and couple to form an N atom to adsorb on the surface and a CO_2 molecule to desorb. The adsorbed N atom further couples with another CO molecule in the gas phase to form an intermediate −NCO on Rh_1; this intermediate can directly couple with an NO molecule adsorbed on the same Rh_1 to form N_2 and CO_2. In another pathway, the adsorbed N atom can couple with a coadsorbed NO on the same Rh_1 to form N_2O; N_2O further reacts with adsorbed CO on the same Rh_1 to form N_2 and CO_2 through a high activation barrier that can be overcome at a high temperature. Our studies show that the singly dispersed metal atoms on an inert support have great potential to perform selective transformation of chemicals. The confirmed catalysis with a singly dispersed Rh_1 on SiO_2 through a mechanism different from a metal nanoparticle supported on the same substrate suggests the significance of taking the single-atom catalysis (SAC) into fundamental studies of catalysis of a supported metal catalyst, since metal nanoparticles and singly dispersed metal atoms likely coexist on the inert support of many supported catalysts.

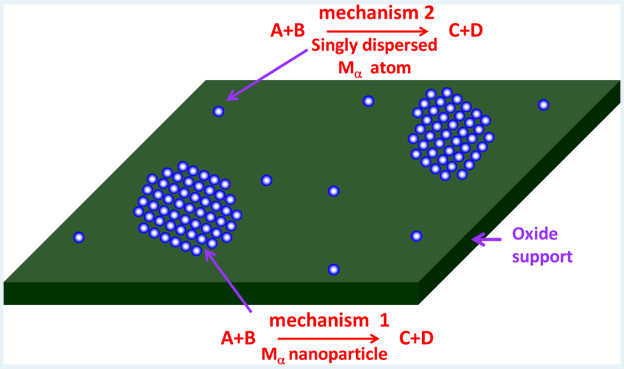

KEYWORDS: *singly dispersed metal atom, single-atom catalysis, insert support, reduction of nitric oxide, rhodium, density functional theory, in situ, operando, infrared spectroscopy*

1. INTRODUCTION

While macroscopically heterogeneous catalysis is a chemical process performed on a solid material, microscopically a single catalytic event is performed on a catalytically active site at the subnanoscale or nanoscale.[1,2] This is because a catalytic event is performed on a catalytically active site typically involving two or a few catalyst atoms. In many cases, a catalytically active site consists of atoms from both a metal nanoparticle and its support; for instance, atoms of a catalytically active site of a bifunctional catalyst, CeO_2 with supported Pt atoms for the water-gas shift

Received: June 1, 2017
Revised: October 10, 2017
Published: October 19, 2017

DOI: 10.1021/acscatal.7b01788
ACS Catal. 2018, 8, 110−121

reaction, include Pt atoms for CO adsorption and surface lattice oxygen atoms and oxygen vacancies of CeO_2 for dissociating H_2O to OH groups.[3]

Single dispersion of precious-metal atoms has been demonstrated to be a promising approach to offer a distinctly different catalytic performance.[4] Different types of supported single-atom catalysts (SAC) or single-site catalysts (SSC) were reported in the last several years.[5−26] Most of these reported single-atom catalysts are metal atoms supported on reducible oxides. Active sites of these single-atom catalysts consist of singly dispersed metal atoms and their surrounding atoms; the surrounding atoms are typically surface lattice oxygen atoms or cations of the reducible oxide support. Strictly speaking, catalytically active sites of these single-atom catalysts are not isolated single atoms but sites of supported atoms, as defined previously.[5]

Different from singly dispersed metal atoms anchored on the surface of a *reducible oxide*, singly dispersed metal atoms can be anchored *on an inert oxide*. In this case, the surface of the inert oxide does not participate in the reaction. Thus, a singly dispersed metal atom on an inert support is truly a single atom for catalysis without any support effect. Whether these single-atom catalysts are active or not in a complex reaction has been an important question for the correct understanding of the catalytic performance of metal catalysts supported on inert substrates; this is because scientists had expected that metal nanoparticles and singly dispersed metal atoms *coexist* on the surface of the support in many catalysts a few decades ago,[1,2] although such coexistence was only experimentally proved by advanced electron microscopy techniques recently.[27,28] Scheme 1c shows singly dispersed metal atoms (M_α) anchored on the surface of an inert oxide (M_β-O). When M_α and M_β are in the same or an adjacent period in the periodic table, it is quite challenging to distinguish M_α from M_β with high angle annular dark field scanning transmission electron microscopy (HAADF-STEM). In these cases, extended X-ray absorption fine structure spectroscopy (EXAFS) could be a better technique. However, for a catalyst consisting of both singly dispersed M_α atoms and M_α metal nanoparticles, EXAFS cannot recognize the singly dispersed metal atoms. This is because EXAFS is an average technique which gives the average coordination number and bond length of both singly dispersed metal atoms and metal atoms of nanoparticles. Thus, for a catalyst with both singly dispersed metal sites and metal nanoparticles, HAADF-STEM is an appropriate technique if the metal atoms and atoms of the support can be readily distinguished.

Although the coexistence of singly dispersed metal atoms and metal nanoparticles can be identified through advanced HAADF-STEM techniques,[27,28] significant questions related to these coexisting singly dispersed metal atoms on an inert support have not been addressed. *Whether these singly dispersed metal atoms supported on an inert substrate are active and how they contribute to the overall catalytic performance have not been considered in most cases in the fundamental studies of catalysis on metal nanoparticles supported on a substrate*. In comparison to the interplaying contributing factors to catalysis on supported metal nanoparticles, including size, shape, and composition,[29] the coexistence of single metal atoms and metal nanoparticles supported on the same inert substrate is an additional factor increasing the complexity of supported catalysts.

Rh is a well-known catalyst used for reduction of NO with CO.[30,31] The catalytic mechanism on Rh nanoparticles has been well addressed in the literature.[1,2,30,31] To explore whether singly dispersed Rh atoms anchored on an inert support are also the active sites for this catalytic reaction and how the catalytic mechanism could be different from that for Rh metal nanoparticles, here we prepared a series of supported Rh catalysts on an inert support, SiO_2, with loadings covering low concentrations (0.010−0.030%), at which Rh atoms are singly dispersed, and medium and high concentrations (>0.030%), at which Rh atoms are dispersed as both single atoms and metal nanoparticles.

Catalysts of singly dispersed Rh atoms supported on an inert oxide, SiO_2 (generally termed Rh_1/SiO_2), were prepared with a modified deposition−precipitation method. The single dispersion of Rh atoms was confirmed with aberration-corrected HAADF-STEM and EXAFS. Rh_1/SiO_2 is active for reduction of NO with CO at a temperature of 300 °C and higher. Careful evaluation of the catalytic performance was carried out in a fixed-bed flow reactor in the temperature range of 220−520 °C. The integration of in situ/operando characterization and density functional theory (DFT) calculations suggests that the first step of catalysis occurs via a Langmuir−Hinshelwood (L-H) mechanism, where one CO and one NO molecules coadsorb on a singly dispersed Rh atom. The coadsorbed CO and NO molecules couple to generate a CO_2 molecule and an adsorbed N atom, which reacts with a second NO or CO molecule to form the byproduct N_2O an −NCO intermediate, respectively. The −NCO intermediate can spill over from the single Rh sites to SiO_2 to form Si−NCO or couple with adsorbed NO to form N_2 and CO_2. At high temperatures, the formed N_2O could further react with adsorbed CO on the same Rh_1 to form N_2 and CO_2 through a large barrier that can be overcome at a relatively high temperature.

Scheme 1. Surfaces of (a) Metal Oxide Nanoparticles (M_α-O), (b) Metal Nanoparticles (M_α-M_α), and (c) Singly Dispersed Metal Atoms M_α Supported on Inert Oxide (M_β-O)

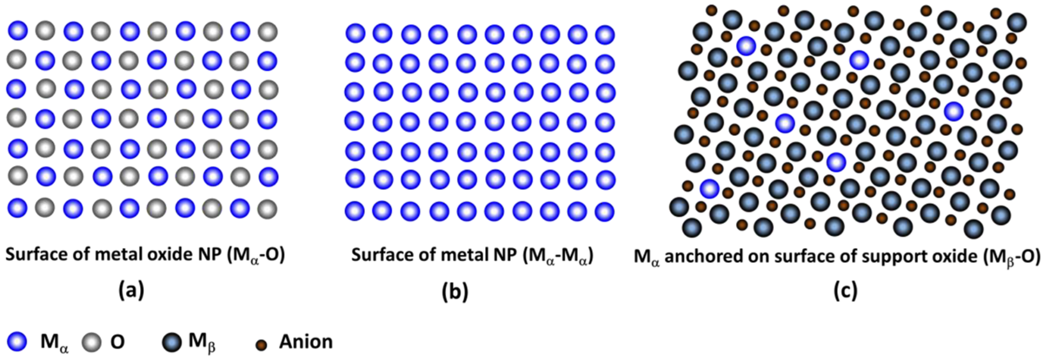
Surface of metal oxide NP (M_α-O) (a)
Surface of metal NP (M_α-M_α) (b)
M_α anchored on surface of support oxide (M_β-O) (c)

2. EXPERIMENTAL SECTION

2.1. Preparation of Rh_1/SiO_2 and Rh NPs/SiO_2 Catalysts. Singly dispersed Rh supported on SiO_2 (Rh_1/SiO_2) and Rh NPs supported on SiO_2 (Rh NPs/SiO_2) were synthesized through a modified deposition−precipitation protocol. In a typical experiment, 0.5 g of fumed SiO_2 (Sigma-Aldrich; used as received) was dispersed in 50 mL of deionized water with the assistance of sonication until a homogeneous translucent solution was obtained. A certain volume of $Rh(NO_3)_3$ aqueous solution (3 mg/mL) prepared by dissolving $Rh(NO_3)_3\cdot 6H_2O$ (Sigma-Aldrich, ∼36% Rh basis; used as received) in deionized water was added using a micropipet while the solution was vigorously stirred. Then, the pH of the solution was gradually adjusted to 9.0 with ammonium hydroxide solution monitored by a pH meter, and the solution was stirred at room temperature for 24 h to reach a thorough equilibrium. The final products were collected by centrifugation, dried under vacuum at 50 °C overnight, and calcined in air at 250 °C for 1 h. The measured concentrations of Rh of as-prepared Rh/SiO_2 samples were determined by inductively coupled plasma atomic emission spectroscopy (ICP-AES, PerkinElmer Optima 3000XL). Samples with Rh weight percentages of 0.010%, 0.017%, 0.030%, 0.050%, 0.18%, and 0.59% were synthesized. All percentages of Rh loading amounts in this paper are by the measured weight unless otherwise indicated.

2.2. Scanning Transmission Electron Microscopy and Extended X-ray Absorption Fine Structure Spectroscopy. Rh_1/SiO_2 and Rh NPs/SiO_2 after catalysis were characterized with an aberration-corrected scanning transmission electron microscope (JEM-ARM200F TEM/STEM) with a guaranteed resolution of 0.08 nm in the HAADF imaging mode. Before microscopy examination, the catalyst powders were ultrasonically dispersed in ethanol and then a drop of the solution was put onto a lacey-carbon-coated TEM Cu grid. Both low- and high-magnification images were extensively screened to extract reliable information on the dispersion of the Rh atoms and/or nanoparticles. EXAFS measurements were performed at the beamline X18B at the National Synchrotron Light Source (NSLS), Brookhaven National Laboratory. The Rh K-edge spectrum (23220 eV) of the catalyst (0.030% Rh/SiO_2) was measured in fluorescence mode under ambient conditions. The Rh K-edge spectrum of a metallic Rh foil was collected at the same time in reference mode for X-ray energy calibration and data alignment. Data processing and analysis were performed with the IFEFFIT package using standard procedures.

2.3. In Situ Infrared Spectroscopy. In situ track of vibrational signatures of surface species under different conditions using infrared spectroscopy was carried out on a Nicolet Nexus 670 FTIR spectrometer using an MCT/A detector with a spectral resolution of 4 cm^{-1} integrated with a diffuse reflectance reaction cell (Pike Technologies, Model HC-900). The gas-switching experiment was performed using an Agilent Cary 670 FTIR equipped with a linearized MCT detector, a Harrick diffuse reflectance accessory, and a Praying Mantis high-temperature reaction cell. Rh/SiO_2 (0.017%) was used without any dilution, and all spectra were acquired under conditions identical with catalytic performance measurements in a gaseous environment at a certain temperature.

2.4. Measurement of Catalytic Performance. Measurements of the catalytic activity and selectivity of the as-prepared catalysts were carried out in a temperature-programmed fixed-bed tubular quartz flow reactor at atmospheric pressure (i.d. 6 mm). A 10 mg portion of the catalyst diluted with 2 g of quartz sand was packed between two glass wool plugs. The bed height was ∼10 mm. Prior to the measurement, the catalyst was pretreated in 5% H_2/Ar at 300 °C for 1 h. The reactant gas mixture consisting of 1.5% NO and 4.5% CO balanced with Ar (NO:CO molar ratio 1:3) was flowing through the catalyst bed at a rate of 90 mL/min. The effluent gas was analyzed with an online gas chromatograph (8610C, SRI Instruments) equipped with a thermal conductivity detector (TCD) for the analysis of both the reactants and products. The measurements of catalytic activity for the reduction of NO with CO and selectivity for producing N_2 from NO were performed at 220−520 °C. There is no activity at a temperature lower than 220 °C for all catalysts studied in this work. Conversion of NO was calculated with the equation

$$C_{NO}\ (\%) = \frac{N_{NO} - N'_{NO}}{N_{NO}} \times 100$$

in which N_{NO} represents the number of moles of NO introduced per minute before catalysis and N'_{NO} stands for the number of moles of NO detected per minute at the downstream of the reactor at a reaction temperature. Selectivity to the production of N_2 was calculated with the equation

$$S_{N_2}\ (\%) = \frac{2N'_{N_2}}{N_{NO} - N'_{NO}} \times 100$$

in which N'_{N_2} is the number of moles of N_2 per minute detected at the downstream of a reactor at a reaction temperature. During the catalytic process, no products other than N_2, N_2O, and CO_2 were detected.

2.5. Computational Modeling. A supercell slab model was built based on the β-cristobalite structure, whose bulk density and refractive index are close to those of amorphous SiO_2.[32−36] A β-cristobalite (111)-$p(2\times 2)$ surface slab ($a = b = 10.12$ Å) was used to model the amorphous SiO_2 surface. Both the top surface and bottom surface of the slab were terminated by oxygen atoms saturated with hydrogen atoms to maintain the chemical valence of Si atoms.[37,38] The slab consists of 13 atomic layers, where the bottom three atomic layers and bottom hydroxyl groups were frozen while the remaining layers were allowed to relax during the calculations. All of the supercell slabs were repeated periodically with a 15 Å vacuum layer between the images in the direction perpendicular to the surface. The Rh atom was attached to the slab model by replacing one silanol. It is noted that the adsorption energy of single-atom Rh is difficult to calculate due to the absence of accurate energy of the replaced Si−OH.

The DFT calculations were performed with the CP2K package.[39] The exchange-correlation energy was described by the generalized-gradient approximation (GGA) with spin-polarized Perdew−Burke−Ernzerhof (PBE) functional.[40] The wave functions were expanded in optimized double-ζ Gaussian basis sets and plane wave basis sets with a cutoff energy of 425 Ry.[41,42] Core electrons were modeled by Geodecker−Teter−Hutter (GTH) pseudopotentials with 4, 6, 17, 5, and 4 valence electrons for Si, O, Rh, N, and C, respectively.[43] Only the gamma point was used to sample the Brillouin zone. The optimizations of the transition states were performed by using the dimer method with a convergence criterion for the maximum force of 4.5×10^{-4} atomic units.[44−47] Vibrational frequency analysis was further used to confirm the transition states with only one imaginary frequency. The reaction energy (ΔE) was defined as the energy difference between the final and initial states. The energy barrier (E_a) was determined as the energy difference between the corresponding transition and initial states.

3. RESULTS AND DISCUSSION

3.1. Single Dispersion of Rh Atoms on SiO_2. Inert supports SiO_2 with anchored singly dispersed Rh atoms or/and Rh NPs were prepared for experimental studies of this work. Since Rh and Si differ significantly in atomic number, Rh atoms can be readily distinguished from SiO_2 with HAADF-STEM.[48] Rh single atoms or nanoparticles appear as high contrast spots or regions in aberration-corrected HAADF-STEM images. Figure 1a presents a large area image of a used catalyst, 0.017% Rh/SiO_2, with SiO_2 particles (10−20 nm) anchored with 0.017% of Rh. No Rh nanoparticle appears in the HAADF image (Figure 1a), although Rh nanoparticles supported on SiO_2 can be readily identified if they exist. An examination of different areas clearly reveals bright spots of Rh atoms on the support. Figure 1b−d shows the representative HAADF-STEM images collected from the used catalyst 0.017% Rh/SiO_2. HAADF-STEM studies suggest that these Rh atoms anchored on the used 0.017% Rh/SiO_2 retained their single dispersion.

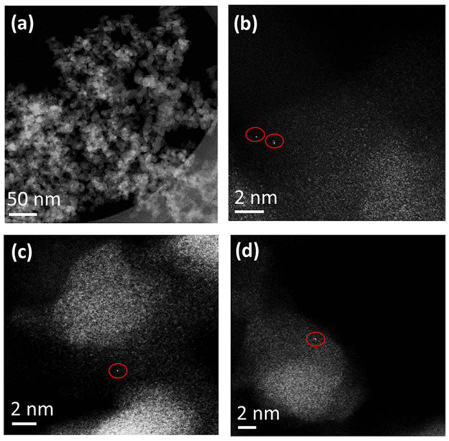

Figure 1. Aberration-corrected HAADF-STEM images of the 0.017% Rh/SiO_2 after catalysis: (a) large-scale image; (b−d) high-resolution STEM images visualizing singly dispersed Rh atoms anchored on SiO_2 marked in red circles.

It is understood that HAADF-STEM is a microscopic technique which could only image a small portion of a transmission electron microscopy (TEM) sample of a catalyst. To check the single dispersion in the *whole* catalyst at the scale of 100 mg, it is necessary to characterize the catalyst with an ensemble technique such as EXAFS to provide average information on the whole catalyst. Particularly, the integration of a microscopic technique providing local information at an atomic scale and an ensemble technique offering average information on all parts of a catalyst would allow us to identify the dispersion and coordination environment of Rh atoms on the inert oxide SiO_2. As the Rh concentrations of 0.010% and 0.017% are lower than the detection limit of beamline X18B at the NSLS, 0.030% Rh/SiO_2 was prepared by exactly the same preparation method used for 0.010% Rh/SiO_2 and 0.017% Rh/SiO_2. The 0.030% Rh/SiO_2 pretreated in 5% H_2/Ar at 300 °C for 1 h was examined ex situ under ambient conditions. As shown in Figure 2a, XANES of the Rh K-edge at 23230 eV clearly shows that Rh atoms are in an oxidized state. In addition, the increase of absorption intensity of the Rh K-edge in the region of 2320 and 2350 eV results from an increasing number of unoccupied local electronic density of states (DOS) of the 4d orbitals (blue line in Figure 2a) due to the transfer of electron density from the Rh to the O atom in contrast to Rh foil (black line in Figure 2a). This enhanced absorption in Figure 2a is also consistent with the presence of oxidized Rh reported in the literature.[49]

The k^2-weighted Rh K-edge EXAFS spectra in k space and r space by Fourier transform for the 0.030% Rh/SiO_2 are shown in Figure 2b,c, respectively. A preliminary visual examination from Figure 2c revealed a dominant peak at 1−2 Å, which suggests a clear Rh−O bonding. The lack of evident peaks at >2 Å in r space (Figure 2c) suggests the absence of Rh−Rh bonding of metal NPs and Rh−O−Rh bonding in the second neighboring shell of rhodium oxide nanoparticles. The fitting of the fine-structure spectrum gave the coordination number (CN) of O to Rh as 5 (Table 1). The lack of both an Rh−Rh metal bond and the second shell of the Rh atom (Rh−O−Rh) in rhodium oxide

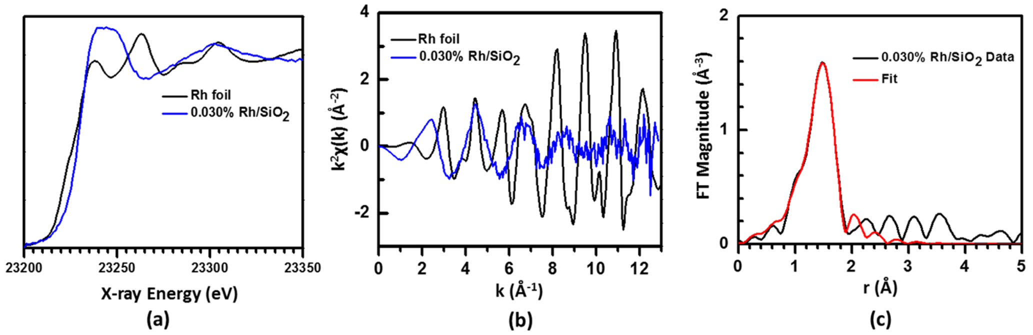

Figure 2. EXAFS studies of 0.030% Rh/SiO_2 after H_2 treatment at 300 °C and catalysis: (a) Rh K-edge XANES data of 0.030% Rh/SiO_2 (blue line) and Rh foil (black line); (b) data of k^2-weighted Rh K-edge EXAFS data in k-space of 0.030% Rh/SiO_2 (blue line) and Rh foil (black line); (c) data of k^2-weighted Rh K-edge EXAFS data in r space of 0.030% Rh/SiO_2 (black line) and the theoretical fit (red line). Coordination numbers of oxygen atoms to Rh_1 and O−Rh bond lengths are given in Table 1.

Table 1. Results of Quantitative Analyses for Rh−O, Rh−Rh, and Rh−Si Contributions of the ex Situ EXAFS Spectrum of 0.030% Rh/SiO_2 after Pretreatment in 5% H_2/Ar at 300 °C for 1 h and Catalysis[a]

Rh/SiO_2	CN(Rh−O)	CN(Rh−Rh)	CN(Rh−Si)	R(Rh−O), Å	σ^2(Rh−O), Å^2
ex situ	4.97 ± 0.37	0	0	2.017 ± 0.007	0.0037 ± 0.00010

[a] No Rh−Rh bonding was observed, suggesting that Rh atoms were singly dispersed.

nanoparticles (Figure 2c) suggests that Rh atoms are indeed singly dispersed on SiO_2. Notably, there is no direct bonding of Rh to Si atoms (Table 1), although 0.030% Rh/SiO_2 was pretreated in 5% H_2/Ar at 300 °C. This suggests that the oxygen atoms between a singly dispersed Rh atom and nearest Si atoms of the surface of SiO_2 were not removed. Thus, Rh_1/SiO_2 is different from the reported Rh_1Co_3/CoO_{1-x} catalyst,[19] in which the singly dispersed Rh atoms directly bond to Co atoms through the formed Rh−Co bonds after H_2 treatment. In the case of 0.030% Rh/SiO_2, EXAFS studies show that Rh atoms only bond with O atoms instead of any Si atoms. To form a Rh−Si bond, surface lattice oxygen atoms of SiO_2 need to be removed to form oxygen vacancies, by which Rh atoms could potentially fill this oxygen vacancy to form a Rh−Si bond. However, at a reduction temperature of 300 °C in 5% H_2/Ar, it is impossible to form an oxygen vacancy on SiO_2, although oxygen vacancies can be readily generated on Co_3O_4,[19,22,23,50] Fe_3O_4,[5] and CeO_2[3,51] at temperatures lower than 250 °C. Therefore, it is reasonable to conclude that no Rh−Si bonds were formed on 0.030% Rh/SiO_2 treated in 5% H_2/Ar at 300 °C.

Dispersion of Rh atoms of Rh/SiO_2 catalyst with a concentration higher than 0.030% after catalysis was checked by the aberration-corrected HAADF-STEM technique. As shown in Figure 3a, high-contrast nanoparticles on 0.50%Rh/SiO_2 were identified. In comparison to Figure 1a, the observation of high-contrast nanoparticles on 0.050% Rh/SiO_2 shows that Rh atoms were aggregated after catalysis at temperatures up to 520 °C. In fact, other than the formation of Rh nanoparticles, singly dispersed Rh atoms supported on SiO_2 were also identified in the HAADF-STEM images of the used 0.050% Rh/SiO_2 catalyst (Figure 3b−d). These observations clearly show that the used 0.050% Rh/SiO_2 consisted of both Rh nanoparticles with a size of 1−2 nm and singly dispersed Rh atoms. In fact, the coexistence of metal nanoparticles and singly dispersed metal atoms on supports has been reported on other catalysts.[27,28] Thus, through EXAFS studies of the used 0.030% Rh/SiO_2 (Figure 2) and HAADF-STEM studies of the used 0.017% Rh/SiO_2 (Figure 1) and the used 0.050% Rh/SiO_2 (Figure 3), 0.030% is close to the upper limit of Rh loading for maintaining single dispersion of all Rh atoms anchored on SiO_2, since the single dispersion of 0.030% Rh/SiO_2 was suggested by EXAFS and no Rh NPs were observed on 0.030% Rh/SiO_2. As expected, at a higher Rh concentration of 0.18% Rh/SiO_2 (Figure 4), Rh atoms aggregated and larger Rh nanoparticles with a size of ∼3 nm were formed. Figure 4d is a high-resolution TEM image of a representative Rh nanoparticle supported on SiO_2. The interplanar distance of 0.19 nm measured in the high-resolution bright field image of a Rh nanoparticle corresponds to the interplanar distance of Rh (200) (Figure 4d). This clearly shows the formation of Rh metallic nanoparticles after catalysis.

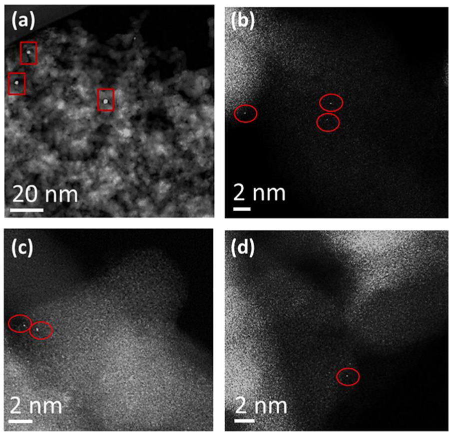

Figure 3. Aberration-corrected HAADF-STEM images of used 0.050% Rh/SiO_2 after catalysis, where the catalyst consists of both Rh nanoparticles and singly dispersed Rh atoms: (a) large-scale image, where Rh nanoparticles were observed and marked with red rectangles; (b−d) high-resolution STEM images visualizing singly dispersed Rh atoms on 0.050% Rh/SiO_2 marked with red circles. All insets in (a)−(d) are representative images of the same TEM sample.

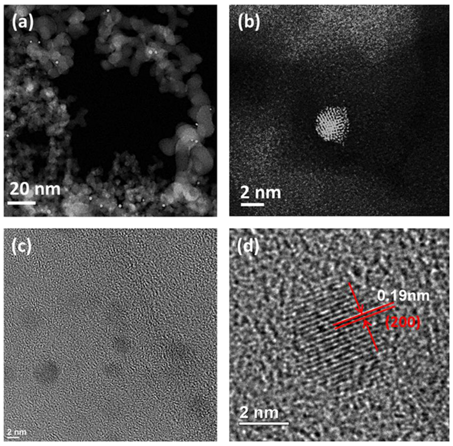

Figure 4. TEM images of used 0.18% Rh/SiO_2 after catalysis: (a) large-scale STEM image; (b) high-resolution STEM image of a random Rh nanoparticle formed after catalysis; (c) large-scale bright-field TEM image; (d) high-resolution TEM image of a random Rh nanoparticle formed after catalysis, where the measured interplanar distance of Rh nanoparticles on SiO_2 corresponds to the (200) plane of metallic Rh.

The used 0.59% Rh/SiO_2 was also examined with HAADF-STEM. As shown in Figure 5a, Rh nanoparticles with a size of 2−3 nm were formed upon catalysis. To reveal the chemical identity of the high-contrast spots in Figure 5a, EDXs of a high-contrast spot in the HAADF image (Figure 5a) marked as Spot 1 and the regular contrast area marked as Spot 2 were analyzed. Clearly, Spot 1 (the bright spot) has chemical elements of Rh,

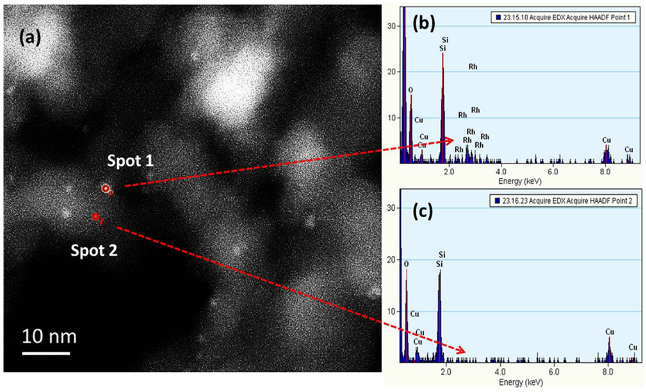

Figure 5. TEM studies of used 0.59% Rh/SiO_2 after catalysis: (a) large-scale STEM image; (b) EDX spectrum collected at the location of Spot 1, where a Rh nanoparticle was readily identified; (c) EDX spectrum at the location of Spot 2 without any Rh nanoparticles. The comparison of the two EDX mappings confirmed that the assignment of high-contrast Spot 1 to Rh nanoparticles is reasonable.

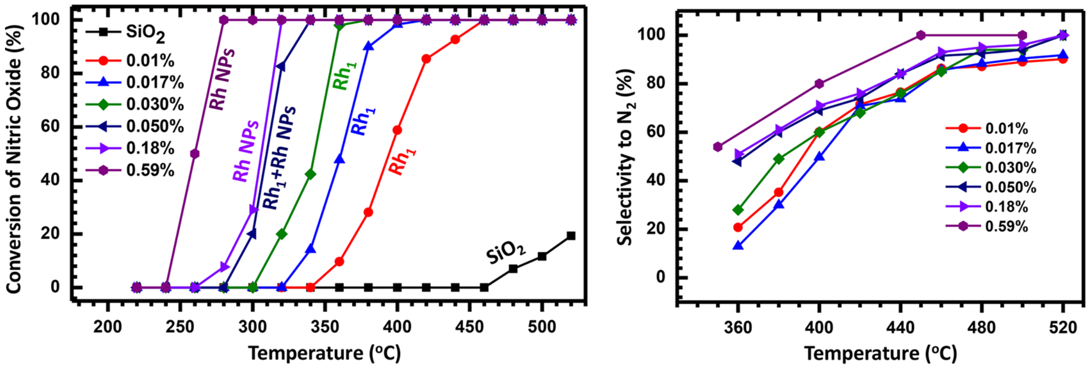

(a) (b)

Figure 6. Catalytic performance of reducing NO with CO in the temperature range of 220−520 °C: (a) catalytic activities in terms of conversion of NO and (b) selectivities for producing N_2 on pure SiO_2 support, 0.010% Rh/SiO_2, 0.017% Rh/SiO_2, 0.030% Rh/SiO_2, 0.050% Rh/SiO_2, 0.18% Rh/SiO_2, and 0.59% Rh/SiO_2.

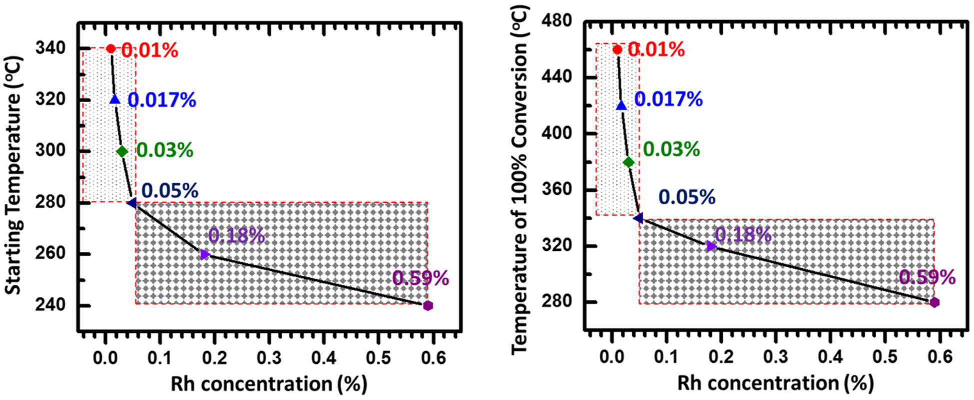

(a) (b)

Figure 7. Temperature of starting catalysis and temperature of 100% conversion of NO on catalysts consisting of inert support, SiO_2, and singly dispersed Rh_1 atoms or/and Rh nanoparticles as a function of total loading of Rh: (a) starting temperature of conversion of nitric oxide; (b) temperature where 100% conversion of NO is reached ($T_{100\%}$) as a function of Rh concentration of Rh/SiO_2.

Si, and O (Figure 5b), while Spot 2 (the dark spot) only has Si and O (Figure 5c). This difference clearly suggests that Spot 1 in HAADF-STEM is definitely contributed by a Rh nanoparticle.

3.2. Catalytic Performances of Singly Dispersed Rh_1 Atoms and Rh Nanoparticles Supported on SiO_2.

Catalytic performances of 0.010% Rh/SiO_2, 0.017% Rh/SiO_2, 0.030% Rh/SiO_2, 0.050% Rh/SiO_2, 0.18% Rh/SiO_2, and 0.59% Rh/SiO_2 for reduction of NO with CO in the temperature range of 220−520 °C were studied in parallel under the exactly same catalytic conditions in the same fixed-bed flow reactor. Figure 6a presents the conversion of NO on different catalysts as a function of reaction temperature. It is noted that there is no activity of pure SiO_2 at temperatures of 460 °C and lower (black line of Figure 6a). Figure 7a presents the starting temperatures of catalysis of these catalysts with different loading levels of Rh. Clearly, the starting temperature decreases along with an increase in the loading amount of Rh. Basically, we can categorize them into a high-temperature regime (starting temperature (at which catalysis activity is observed) >300 °C marked with a box filled with dots) and a low-temperature regime (starting temperature ≤300 °C marked with another box). Since Rh atoms of 0.010%, 0.017%, and 0.030% Rh supported on SiO_2 are singly dispersed on the inert support SiO_2, the activities of these catalysts are solely contributed by the number of these singly dispersed Rh atoms. Figure 7 shows that singly dispersed Rh atoms on SiO_2 are not active at temperatures lower than 300 °C. Another loading-dependent evolution of the series of Rh/SiO_2 catalysts is the temperature where conversion of NO reaches 100%; $T_{100\%}$ of those catalysts increases along with a decrease in loading of Rh.

In addition to the difference in the catalytic activity, the selectivity for production of N_2 on singly dispersed Rh atoms is different from that of Rh nanoparticles. Figure 6b shows the selectivity for production of N_2 on Rh/SiO_2 with different loadings of Rh. For each of these catalysts, clearly the selectivity for production of N_2 increases along with an increase in the reaction temperature. The red circle marks the selectivity for producing N_2 on singly dispersed Rh sites of 0.010% Rh/SiO_2, 0.017% Rh/SiO_2, and 0.030% Rh/SiO_2 (Figure 6b). At the low-temperature regime (<420 °C), catalytic selectivity for production of N_2 is lower than that of Rh/SiO_2 with a relatively high loading.

3.3. In Situ/Operando IR Studies of Reduction of NO with CO on Rh_1/SiO_2.

In order to gain a fundamental understanding of the catalytic mechanism of singly dispersed Rh sites on SiO_2, diffuse reflectance infrared Fourier transform spectroscopy (DRIFTS) was performed to probe the adsorption state of reactants and reaction intermediates under different reaction and catalytic conditions. Due to the overlap of NO adsorption bands with the strong background of amorphous SiO_2 support at 1300−1800 cm^{-1}, it is extremely challenging to obtain clear NO adsorption signatures at different conditions. Thus, the NO adsorption bands (1300−1800 cm^{-1}) are not presented.

DOI: 10.1021/acscatal.7b01788
ACS Catal. 2018, 8, 110−121

To probe the adsorption of reactant molecules, an experimental method of switching reactant gas was performed. In this method, 0.017% Rh/SiO_2 was first pretreated with H_2 at 300 °C. After this pretreatment, the catalyst was exposed to CO at room temperature, followed by purging of CO with He. It is noted that the chemisorbed CO molecules remained on the surface, although gas-phase CO was completely purged. Subsequently NO was introduced to the reactor and the catalyst remained in NO. Vibrational signatures of reactant-relevant species on 0.017% Rh/SiO_2 in NO gas were collected as a function of time. Notably, the moment when NO was introduced to the catalyst (0.017%Rh/SiO_2) was defined to be $t = 0$ in Figure 8a.

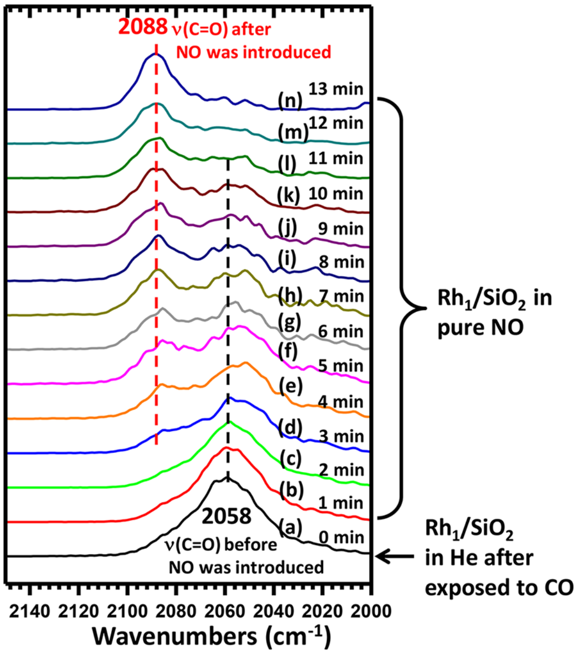

Figure 8. In situ IR studies of the evolution of adsorbed CO molecules on 0.017% Rh/SiO_2 at room temperature. The catalyst was first exposed to pure CO and purged with He at $t = 0$ min. Then, NO was introduced and IR spectra were collected thereafter (0−13 min).

At the moment that NO was introduced, we started to count time ($t = 1, 2, ...$ min). At $t = 0$ min, the adsorbed CO exhibits a wide peak at ~2058 cm^{-1} (Figure 8a), which is attributed to the C−O stretching vibration of linear CO adsorption on Rh before NO was introduced.[52] Upon the introduction of NO for 3 min (Figure 8d), the intensity of the C−O band at ~2058 cm^{-1} progressively diminished and a new band of CO appeared at ~2088 cm^{-1}. The observation of the new band at 2088 cm^{-1} suggests (1) the coadsorption of NO molecules and (2) a greatly modified adsorption state of the originally chemisorbed CO molecule on the singly dispersed Rh atom by the coadsorbed NO molecules. The variation in the binding strength of chemisorbed CO molecules upon coadsorption of NO can be rationalized with less back-donation of electron density from Rh atoms to a chemisorbed CO molecule. When NO adsorbs on a Rh atom with an originally adsorbed CO, some of the electron density of Rh 4d that had been originally back-donated to the antibonding orbital of C−O bond was then back-donated to the antibonding orbital of the N−O bond. Thus, the reduced Rh 4d back-donating to the antibonding orbital of C−O leads to a stronger C−O bond and a weaker Rh−C bond in contrast to the originally chemisorbed CO molecule on Rh_1. As a result, the C−O stretching frequency upshifts from ~2058 cm^{-1} (adsorption without NO molecules) to ~2088 cm^{-1} (coadsorption with a NO molecule). This upshift of vibrational signatures of CO from 2058 to 2088 cm^{-1} shows that (1) the NO molecule did chemisorb on the surface of the catalyst, (2) the CO molecule remained on the Rh_1 atom, and (3) the binding strength of CO to Rh_1 decreased upon adsorption of NO. These insights suggest that NO and CO coadsorb on Rh_1 supported on SiO_2.

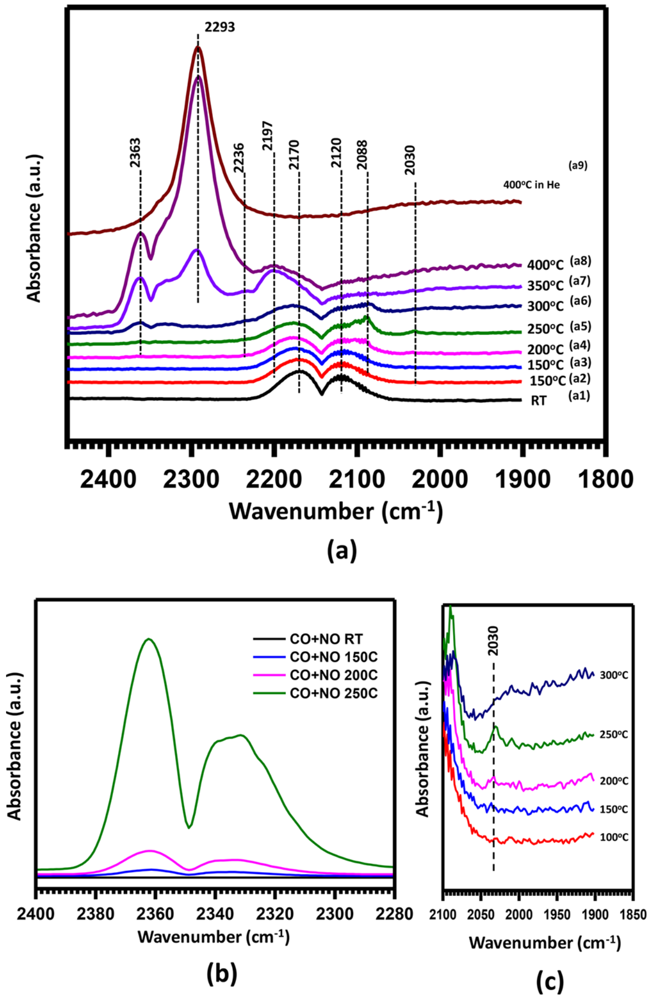

Figure 9. In situ/operando studies of surface species on single atoms Rh_1 supported on SiO_2: (a) in situ IR studies of the evolution of surface species on 0.017% Rh/SiO_2 in a flowing mixture of 1.5% NO and 4.5% CO balanced with He during catalysis; (b) enlarged IR spectra in the 2400−2280 cm^{-1} region in a reactant gas mixture at room temperature and 150, 200, and 250 °C, showing clear formation of CO_2; (c) enlarged IR spectra in the 2100−1900 cm^{-1} region in a reactant gas mixture at 100, 150, 200, 250, and 300 °C, showing the signature region of *gem*-dicarbonyl $[Rh^+(CO)_2]$.

Vibrational signatures of adsorbates/intermediates of 0.017% Rh/SiO_2 during catalysis in the mixture of CO and NO at different catalysis temperatures were tracked with IR. Figure 9a presents the IR spectra collected from 2500 to 1900 cm^{-1} as a function of catalysis temperature. The peaks of gas-phase CO at 2170 and 2120 cm^{-1} were clearly observed at 25 °C (Figure 9a1), well consistent with the literature.[53] In addition, the characteristic vibrational double peaks of product molecules[53] CO_2 in the region of 2280−2400 cm^{-1} can be readily detected at 150 °C, as shown in Figure 9b, although they were not obvious in Figure 9a. Importantly, here the observation of CO_2 molecules suggests that the coadsorbed CO and NO on a single Rh atom can react and then form a CO_2 molecule at 150 °C.

When the temperature was raised above 200 °C (Figure 9a4), two vibrational peaks at ∼2088 and ∼2030 cm^{-1} emerged and kept increasing at 250 °C (Figure 9a5). On the basis of the data of Figure 8, the vibrational signature at ∼2088 cm^{-1} is well consistent with that of chemisorbed CO when NO is coadsorbed on Rh_1. The emergence of a new peak at ∼2030 cm^{-1} (Figure 9a5) accompanied by 2088 cm^{-1} (Figure 9c) suggests the formation of rhodium *gem*-dicarbonyl at 150−250 °C, on the basis of reference IR studies of $[Rh^+(CO)_2]$.[53,54] Thus, the vibrational features at 2088 and 2030 cm^{-1} identified on 0.017% Rh/SiO_2 at 200−250 °C in the mixture of NO and CO (Figure 9a4,a5) are contributed by (1) adsorbed CO molecules on singly dispersed Rh atoms with coadsorbed NO molecules and (2) the formed *gem*-dicarbonyl $[Rh^+(CO)_2]$, respectively. These assignments and observations confirm the assumption that a singly dispersed Rh atom on SiO_2 can simultaneously adsorb two reactant molecules (Figure 9a).

As shown in Figure 9a at temperatures higher than 300 °C, vibrational features of surface species are distinctly different from those at 300 °C or lower. As shown in the enlargement of the region of 2000−2060 cm^{-1} in Figure 9c, the adsorption signature of $[Rh^+(CO)_2]$ at 2030 cm^{-1} gradually disappeared. However, along with the disappearance of $[Rh^+(CO)_2]$, new species at 2363 cm^{-1} in Figure 9a6−a8 formed simultaneously. On the basis of the literature,[53] this species is an adsorbed N_2O molecule. The identified temperature (∼300−350 °C) at which the $[Rh^+(CO)_2]$ species (2030−2088 cm^{-1}) disappeared and CO_2 (2280−2400 cm^{-1}) and N_2O (2363 cm^{-1}) formed is consistent with the starting temperature of NO conversion on 0.017% Rh/SiO_2 of 320 °C (Figure 7a).

The appearance of the vibrational band at 2197 cm^{-1} at 350 °C (Figure 9a7) is consistent with the reported vibrational band of −NCO intermediate adsorbed on Rh sites (Rh−NCO) in the literature.[53,54] The intensity attenuation of $\nu_{\text{Rh-NCO}}$ at 2197 cm^{-1} at 400 °C is in line with the feature of evolution of a stable intermediate. In addition, a peak at 2293 cm^{-1} was clearly observed at 350 °C. It is assigned to an −NCO species adsorbed on Si sites (Si−NCO) on the basis of the literature.[54] Notably, this Si−NCO vibration (2293 cm^{-1}) is quite different from that of Rh−NCO (2197 cm^{-1}).[53,54] In contrast to the decay of −NCO adsorbed on Rh atoms (2197 cm^{-1}) along with an increase in catalysis temperature from 300 to 400 °C, the intensity of −NCO species adsorbed on SiO_2 was largely enhanced. The decreased intensity of Rh−NCO and simultaneous increase of NCO bound to SiO_2 suggests a correlation between the two types of NCO species. As the SiO_2 support is inert in the reaction of NO and CO, the observed Si−NCO must be driven from a spillover of −NCO species from their original sites (Rh atoms) to SiO_2 support at temperatures higher than 300 °C. According to our spectra, the intensity of this band at 2293 cm^{-1} was accumulated at high temperature and this species did not desorb or decompose at 400 °C (Figure 9a9). This high stability of the Si−NCO shows that −NCO adsorbed on SiO_2 is only a spectator.

The sequential reactant-switching experiment performed in Figure 10 further supports the above assignment of absorption bands. All of these studies in Figure 10 were performed on the same catalyst at the same temperature, 350 °C. Figure 10a is the vibrational spectrum of the surface of 0.017% Rh/SiO_2 at 350 °C in a mixture of CO and NO. When CO was purged and NO remained in the flowing reactor, all peaks except 2293 cm^{-1} disappeared (Figure 10b). As discussed above, the remaining peak at 2293 cm^{-1} in NO gas is assigned to Si−NCO. When NO was purged and He was introduced at 350 °C (Figure 10c), the Si−NCO still remained. Since 0.017% Rh/SiO_2 is active at 350 °C, Si−NCO is assigned as a spectator robustly binding to the SiO_2 surface. After NO and CO were introduced to the reactor again (Figure 10d), the vibrational features of adsorbed CO_2 at 2363 cm^{-1}, N_2O at 2236 cm^{-1}, and Rh−NCO at 2197 cm^{-1} were observed again. After NO was purged and only CO remained in the flowing reaction cell, the absorption peaks of adsorbed CO_2 at 2363 cm^{-1}, N_2O at 2236 cm^{-1}, and Rh−NCO at 2197 cm^{-1} disappeared (Figure 10e). The disappearance of Rh−NCO at 2197 cm^{-1} and conservation of Si−NCO at 2293 cm^{-1} confirm that Rh−NCO is an intermediate but −NCO is bound to SiO_2.

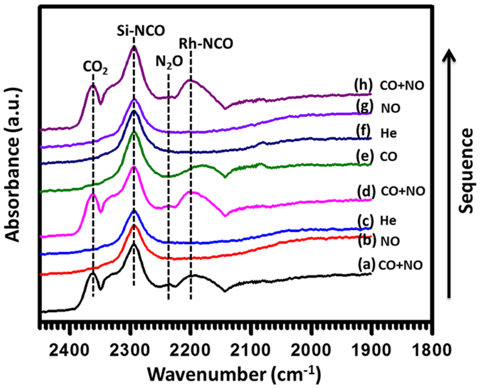

Figure 10. In situ IR studies of the evolution of surface species on 0.017% Rh/SiO_2 at 350 °C in different gaseous environments.

3.4. Interpretation of Reaction Mechanism of Reduction of NO with CO on Rh_1/SiO_2 at a Molecular Level. To explore the various feasible adsorption and reaction mechanisms of NO reduction with CO on singly dispersed Rh_1 atoms anchored on inert oxide, computational modeling of the adsorption, activation, and reaction pathway using periodic density functional theory (DFT) was performed.

3.4.1. Structure of Rh_1 Single Site on SiO_2. After the structural optimization, the Rh_1 atom binds strongly with three oxygen atoms in the *β*-cristobalite (111) surface, with an average bond length of 1.88 Å. It is known that normal Rh−O bond length is ∼1.9 Å, which is shorter than the ∼2.02 Å observed in experiments by EXAFS. Since the bond length revealed by EXAFS is an average one, it indicates that there are other oxygen species weakly binding to the Rh_1 atom. EXAFS studies of the post-reaction catalyst (0.030% Rh_1/SiO_2) were performed ex situ. It is possible that atmospheric water molecules were adsorbed on these Rh sites once the catalyst was exposed to ambient conditions. In addition, we cannot neglect that the sample used in experiment is amorphous SiO_2. Thus, it is also possible for single-atom Rh to connect with other silanols by coordination bonds. Here water molecules were used just to simulate the coordination bond simply. With regard to the number of water molecules, we tested all possible structures, and the results are summarized in Table 2.

Table 2. Calculated Adsorption Energies (eV) and Rh−O Bond Lengths (Å) for Different Models

no. of water molecules	adsorption energy of increased H_2O	av Rh−O bond length	coordination no. of Rh
1	−1.05	1.978	4
2	−1.31	2.024	5
3	−1.11	2.058	6

After calculation, the model with two water molecules is in good agreement with the ex situ EXAFS characterization result of 2.017 ± 0.007 Å (Table 1). Therefore, we chose this model as the local coordination shell of the Rh_1 atom, which is denoted Rh_1O_5 (Figure 11). It should be noted that the number of water molecules does not have a significant effect on subsequent calculations. The coordination bonds can be broken by the coadsorption of NO and CO because the binding energies of CO and NO on Rh_1 (−3.15 eV) are much larger than the adsorption energy of two H_2O molecules (−2.35 eV), which corroborates that the reaction occurs on the single Rh atom binding with three oxygen atoms in the β-cristobalite (111) surface.

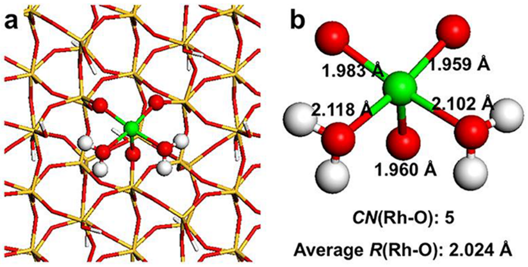

Figure 11. Optimized structure of singly dispersed Rh_1 atoms anchored on inert support SiO_2: (a) top view of the optimized Rh_1/SiO_2 (111) model; (b) bonding environment of the Rh_1 atom. The singly dispersed Rh atom bonds to three oxygen atoms from SiO_2 and two oxygen atoms of two adsorbed water molecules. Distances are shown together with the coordination number (CN).

3.4.2. The reaction mechanism. The calculated energies of intermediates and activation barriers of each proposed elementary step are given in Table 3. Figure 12 presents the energy profile of the reduction of NO with CO on Rh_1/SiO_2 and the optimized structures of corresponding intermediates and transition states. In Table 3 and Figure 12, each elementary step is labeled numerically, with the suffixes A and B representing two different pathways when needed. On the basis of the experimental findings of IR studies, coadsorption of CO and NO is the first step of this reaction. Thus, the catalytic cycle of reducing NO with CO starts with the coadsorption of one NO and one CO molecule on the same singly dispersed Rh atom (step 1). It is noted that the calculated vibrational peak for CO stretching shifts from 2058 to 2072 cm^{-1} upon the adsorption of an NO molecule, in agreement with the IR observations. Further calculations show that the coadsorbed NO* and CO* can couple to form a CO_2 molecule by overcoming a reaction barrier of 2.16 eV (step 2), leaving the N* atom binding to the Rh_1 atom. This high activation barrier (2.16 eV) can well explain why a relatively higher reaction temperature is necessary for reduction of NO with CO on singly dispersed Rh atoms anchored on inert SiO_2.

Table 3. Calculated Reaction Energies (ΔE) and Activation Barriers (E_a) for Elementary Steps in the Reduction of NO with CO on Rh_1/SiO_2[a]

	0 K		600 K	
reaction pathway	ΔE (eV)	E_a (eV)	ΔE (eV)	E_a (eV)
(1) NO + CO → NO* + CO*	−3.15		−0.35	
(2) NO* + CO* → CO_2 + N*	−0.48	2.16	−2.00	2.16
(3A) N* + NO → N* + NO*	−0.62		0.82	
(4A) N* + NO* → N_2O*	−1.45	0.68	−1.45	0.68
(5A) N_2O* → N_2O	0.72		−0.84	
(3B) N* + CO → N* + CO*	−0.77		0.59	
(4B) N* + CO* → NCO*	−1.33	0.68	−1.33	0.68
(5B) NCO* + NO → NCO* + NO*	−1.51		−0.07	
(6B) NCO* + NO* → IM1	0.92	2.01	0.92	2.01
(7B) IM1 → IM2	0.28	0.74	0.28	0.74
(8B) IM2 → N_2* + CO_2	−3.56	0.21	−5.07	0.21
(9B) N_2* → N_2	0.82		−0.50	

[a] The contributions of the entropy term to the free energies of each gas phase were taken from ref 57. These elementary steps can be found in Figure 12.

Upon desorption of CO_2, a chemisorbed N atom remains on the surface. Either the NO or the CO molecule in the gas phase could adsorb on the Rh_1 atom. On the basis of the calculated energy profile in Figure 12, coadsorption of N* and the incoming CO molecule (step 3B) is slightly thermodynamically more favorable than coadsorption of N* and NO (step 3A), while coupling of N* and NO* (TS4A and step 4A) has a barrier similar to that for the coupling of N* and CO* (TS4B and step 4B). Thus, steps 3A and 3B are competitive. In pathway A, the formed N_2O molecule can desorb at a relatively low temperature (step 5A), and the Rh_1 site is available for subsequent catalytic processes. In pathway B, the Rh atom can adsorb another NO molecule from the gas phase after the formation of the Rh−NCO intermediate. The adsorbed NO* can couple with NCO* to form one CO_2 and one N_2 product molecule by overcoming activation barriers of 2.01 eV (TS6B and step 6B), 0.74 eV (TS8B and step 7B), and 0.21 eV (TS8B and step 8B). The desorption energy of the formed N_2 molecule is 0.82 eV, which is slightly larger than that of the N_2O molecule. It is interesting to note that adsorbed NCO* can also spill over from the Rh site to the Si site. The calculated vibrational frequencies of Rh−NCO and Si−NCO are 2171 and 2332 cm^{-1}, respectively, which are consistent with the experimental observations. As a result, the reaction steps on Rh_1/SiO_2 mainly consist of (1) the coadsorption of NO and CO to form first CO_2 (steps 1 and 2), (2) the coupling of N* and NO to form N_2O (steps 3A−5A), and (3) the coupling of N* with CO to form an −NCO species, which can further react with adsorbed NO to form N_2 and second CO_2 (steps 3B−9B).

The energetic span model developed by Kozuch has been applied to compute the turnover frequencies (TOFs) of the catalytic system.[55] According to the energetic span theory, the effective reaction barriers are not the reaction barriers of the rate-determining steps but the energy differences between two rate-determining states in the whole energy profiles. Thus, TOF can be written as

$$\mathrm{TOF} \approx \frac{k_B T}{h} e^{-E_a^{\mathrm{eff}}/RT}$$

where E_a^{eff} is the effective reaction barrier.

On the basis of the reaction energies and activation barriers under 600 K containing the entropic effects, as given in Table 3, the calculated log TOF under 600 K is −5, which seems much smaller than the experimental result. However, the TOF of Rh nanoparticles has also been calculated using the energetic span model on the basis of the data from Xie et al.[56] At the same temperature (600 K), the TOF of Rh nanoparticles is 800 times as large as that of Rh_1/SiO_2 SAC, agreeing well with the experimental results. Thus, although the calculated TOF is underestimated, the comparison between the Rh nanoparticles and Rh_1/SiO_2 SAC can further affirm our opinion on the reaction mechanism.

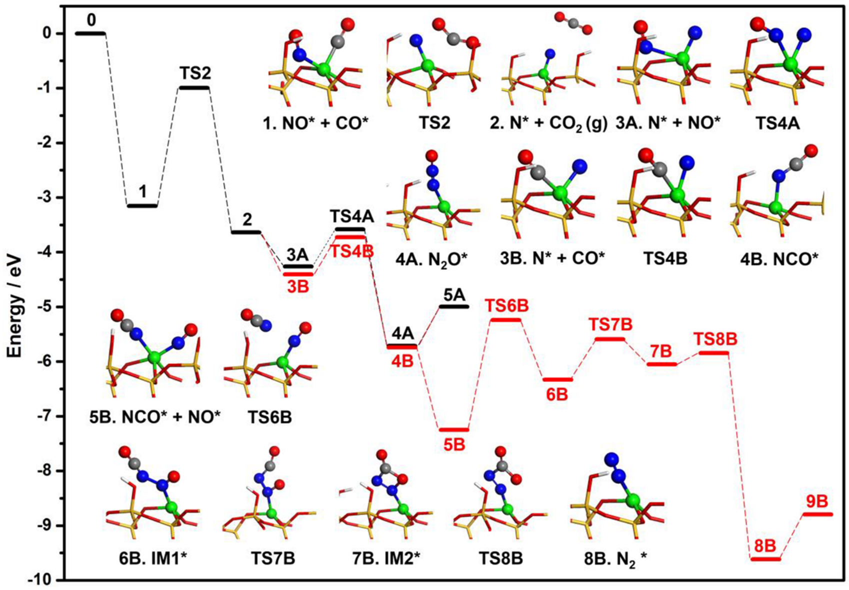

Figure 12. Calculated energy profile of the reduction of NO with CO on Rh_1/SiO_2 and optimized structures of the intermediates and the transition states. Elementary steps are labeled numerically, with suffixes A and B standing for two different possible reaction pathways and TS denoting the transition state. Color code: Rh (green), N (blue), C (gray), and O (red), with the silica support represented by sticks.

3.4.3. Selectivity of N_2. To investigate the selectivity of N_2, we also calculated the reaction path of the reduction of N_2O to the ideal product N_2. The calculated energies of intermediates and activation barriers of each proposed elementary step are given in Table 4. Figure 13 presents the energy profile of the reduction of N_2O to the ideal product N_2 on Rh_1/SiO_2 and the optimized structures of corresponding intermediates and transition states. The cleavage of the N−O bond of the formed N_2O could be performed through coupling N_2O with CO by an Eley−Rideal (E-R) mechanism (steps 6A and 7A) with an activation barrier of 0.97 eV. After the formation of N_2, the remaining O* atom can couple with a coadsorbed CO molecule to form CO_2 with a small barrier of 0.26 eV (step 8A). The energetic span model has also been employed to obtain the TOFs. Considering the entropic effect on gas under 600 K, the effective reaction barrier is 2.53 eV, which is larger than 2.16 eV. Therefore, the product formed at low temperatures is mainly N_2O. With an increase in temperature, the effective barrier for the coupling of N_2O with CO can be overcome more readily, leading to a higher selectivity of N_2.

Table 4. Calculated Reaction Energies (ΔE) and Activation Barriers (E_a) for Elementary Steps in the Reduction of N_2O to Ideal Product N_2[a]

	0 K		600 K	
reaction pathway	ΔE (eV)	E_a (eV)	ΔE (eV)	E_a (eV)
(6A) CO → CO*	−2.05		−0.70	
(7A) CO* + N_2O → N_2 + O* + CO*	−0.31	0.97	−0.07	2.53
(8A) CO* + O* → CO_2	−1.44	0.26	−2.96	0.26

[a] These elementary steps can be found in Figure 13.

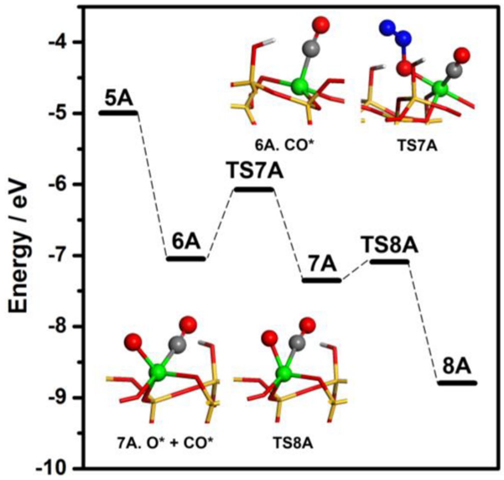

Figure 13. Calculated energy profile of the reduction of N_2O to the ideal product N_2 on Rh_1/SiO_2 and optimized structures of the intermediates and the transition states.

3.4.4. Singly Dispersed Rh Atoms vs Rh Nanoparticles Supported on SiO_2. Theoretically, Rh clusters can be used to model the Rh nanoparticles supported on an inert oxide such as SiO_2. Xie et al. reported the catalytic mechanism in the reduction of NO by CO on the Rh_7^+ cluster.[56] It is found that adsorption of an NO molecule on Rh_7^+ cluster (−1.49 eV) is definitely weaker than that on single-atom Rh (−2.55 eV). However, the coadsorption of NO and CO molecules on the Rh_7^+ cluster (−2.98 eV) is comparable with that on single-atom Rh (−3.15 eV). This is because the Rh_7^+ cluster can provide multiple adsorption sites while single-atom Rh can only accommodate at most two adsorbates. One critical difference between singly dispersed Rh atoms and Rh nanoparticles supported on SiO_2 is the starting temperature. On Rh nanoparticles supported on SiO_2, the starting temperature is lower than that on singly dispersed Rh atoms. Consistent with this difference, the effective barrier for NO conversion on Rh_7^+ cluster is 0.37 eV smaller than that on Rh_1/SiO_2. It is noted that the catalytic reaction of NO reduction with CO on the catalyst of singly dispersed Rh atoms is distinctly different from that on Rh nanoparticles supported on SiO_2. For Rh nanoparticles supported on SiO_2, the key step is the irreversible dissociation of NO, where the dissociated N atom and O atom adsorb on different Rh atoms. However, for $Rh_1/$

SiO_2, NO hardly dissociates with only one active site. The coupling of coadsorbed CO and NO to form CO_2 and adsorbed N atom is the rate-determining step. Another critical difference between singly dispersed Rh atoms and Rh nanoparticles supported on SiO_2 is the selectivity for production of N_2 in the reduction of NO with CO. At the same temperature, Rh nanoparticles supported on SiO_2 have a selectivity higher than that on Rh_1/SiO_2, which also originates from the different mechanisms. For Rh nanoparticles supported on SiO_2, NO molecules dissociate to produce isolated N and O atoms, and then these N atoms couple to form N_2. However, in the case of singly dispersed Rh atoms, the NO molecule cannot dissociate but directly reacts with the remaining N atom produced from the prior coupling of coadsorbed NO and CO molecules to form the N_2O byproduct, and the formed N_2O can be further reduced to N_2 with the help of a CO molecule via an E-R mechanism. The lower activation barrier to form N_2 on the Rh_7^+ cluster leads to the higher selectivity at the same temperature in comparison to Rh_1/SiO_2.

Overall, the significant difference in the reaction mechanisms between singly dispersed Rh atoms and Rh nanoparticles supported on SiO_2 is that an NO molecule can dissociate to N and O atoms directly on Rh nanoparticles due to the multiple adsorption sites, which leads to the higher activity and selectivity on Rh nanoparticles in comparison to that on singly dispersed Rh atoms.

4. SUMMARY

Catalysts of singly dispersed Rh_1 atoms on the inert support SiO_2 were prepared with an Rh loading amount of lower than 0.030%. The single dispersion of Rh_1 atoms was identified with EXAFS and HAADF-STEM techniques. The chemical and coordination environments of Rh atoms were analyzed with EXAFS. This single-atom catalyst catalyzes the reduction of NO with CO with a starting temperature higher than that for Rh nanoparticles supported on SiO_2. In situ IR studies and DFT calculations show that catalytic conversion of NO with CO on the catalyst of singly dispersed Rh atoms is performed through mechanisms distinctly different from those on Rh nanoparticles supported on SiO_2. For Rh_1/SiO_2, two reaction pathways were identified to form different products. Upon the coupling of coadsorbed CO and NO on the singly dispersed Rh atom to form CO_2 and an adsorbed N atom, the adsorbed N atom can couple with a coadsorbed CO to form −NCO bound to Rh_1, which can spill over from the single Rh sites to SiO_2 to form Si−NCO or couple with adsorbed NO to form N_2 and CO_2. On the other hand, the adsorbed N atom could also couple with a coadsorbed NO to form N_2O. In addition, the formed N_2O could further react with adsorbed CO on the same Rh_1 to form N_2 and CO_2 through a large barrier that can be overcome at a high temperature. These integrated in situ studies and DFT calculations show that the singly dispersed metal atoms on the inert support can be active in catalysis through mechanisms quite different from those of metal nanoparticles supported on the same oxide. The confirmed catalytic activity of singly dispersed metal atoms anchored on an inert support suggests that the contribution of singly dispersed metal atoms on an inert support should be taken into account when a fundamental understanding of the catalytic mechanism on a supported metal nanoparticle catalyst is pursued.

■ AUTHOR INFORMATION

Corresponding Authors

*E-mail for J.L.: junli@tsinghua.edu.cn.
*E-mail for F.T.: franklin.feng.tao@ku.edu.

ORCID

Zili Wu: 0000-0002-4468-3240
Tian-Wei Goh: 0000-0002-4141-3392
Wenyu Huang: 0000-0003-2327-7259
Anatoly I. Frenkel: 0000-0002-5451-1207
Jun Li: 0000-0002-8456-3980
Franklin Feng Tao: 0000-0002-4916-6509

Author Contributions

&S.Z. and Y.T. contributed equally.

Notes

The authors declare no competing financial interest.

■ ACKNOWLEDGMENTS

The work started at University of Kansas. Most experimental studies were performed at University of Kansas and this work was mainly funded by Chemical Sciences, Geosciences and Biosciences Division, Office of Basic Energy Sciences, Office of Science, U.S. Department of Energy, under Grant No. DE-SC0014561. S.Z., Y.T., L.N., T.Z., and F.T. were supported by the DOE Grant No. DE-SC0014561. Computational studies were performed in Jun Li group at Tsinghua University. Some IR spectra were collected at Z.W. lab at the Center for Understanding and Control of Acid Gas-Induced Evolution of Materials for Energy (UNCAGE-ME), an Energy Frontier Research Center funded by U.S. Department of Energy, Office of Science, Basic Energy Sciences Energy Sciences. S.Z was partially supported by National Science Foundation under the grant NSF-CHE-1462121. The theoretical work was supported by the National Natural Science Foundation of China to J.L. (NSFC Grant Nos. 91645203 and 21590792). J.(J.)L. acknowledges financial support from the National Science Foundation under CHE-1465057 and the use of the John M. Cowley Center for High Resolution Electron Microscopy at Arizona State University. The calculations were performed by using supercomputers at Tsinghua National Laboratory for Information Science and Technology and the Supercomputing Center of Computer Network Information Center of the Chinese Academy of Sciences. We also acknowledge support from the U.S. Department of Energy Grant No. DE-FG02-03ER15476 and Synchrotron Catalysis Consortium (U.S. Department of Energy, Office of Basic Energy Sciences, Grant No. DE-SC0012335). W.H. and T.-W.G. acknowledge the support from the donors of the American Chemical Society Petroleum Research Fund, for partial support of this research.

■ REFERENCES

(1) Somorjai, G. A.; Li, Y. *Introduction to Surface Chemistry and Catalysis*, 2nd ed.; Wiley: Hoboken, NJ, 2010.

(2) Ertl, G.; Knözinger, H.; Schuth, F.; Weitkamp, J. *Handbook of Heterogeneous Catalysis*; Wiley-VCH: Weinheim, Germany, 2008.

(3) Fu, Q.; Saltsburg, H.; Flytzani-Stephanopoulos, M. *Science* **2003**, *301*, 935−938.

(4) Yang, X. F.; Wang, A. Q.; Qiao, B. T.; Li, J.; Liu, J. Y.; Zhang, T. *Acc. Chem. Res.* **2013**, *46*, 1740−1748.

(5) Qiao, B.; Wang, A.; Yang, X.; Allard, L. F.; Jiang, Z.; Cui, Y.; Liu, J.; Li, J.; Zhang, T. *Nat. Chem.* **2011**, *3*, 634−641.

(6) Flytzani-Stephanopoulos, M.; Gates, B. C. *Annu. Rev. Chem. Biomol. Eng.* **2012**, *3*, 545−574.

(7) Huang, Z.; Gu, X.; Cao, Q.; Hu, P.; Hao, J.; Li, J.; Tang, X. *Angew. Chem.* **2012**, *124*, 4274−4279.

(8) Lu, J.; Aydin, C.; Browning, N. D.; Gates, B. C. *Angew. Chem., Int. Ed.* **2012**, *51*, 5842−5846.

(9) Sun, S.; Zhang, G.; Gauquelin, N.; Chen, N.; Zhou, J.; Yang, S.; Chen, W.; Meng, X.; Geng, D.; Banis, M. N. *Sci. Rep.* **2013**, *3*, 1775.

(10) Flytzani-Stephanopoulos, M. *Acc. Chem. Res.* **2014**, *47*, 783−792.

(11) Guo, X.; Fang, G.; Li, G.; Ma, H.; Fan, H.; Yu, L.; Ma, C.; Wu, X.; Deng, D.; Wei, M. *Science* **2014**, *344*, 616−619.

(12) Kistler, J. D.; Chotigkrai, N.; Xu, P.; Enderle, B.; Praserthdam, P.; Chen, C. Y.; Browning, N. D.; Gates, B. C. *Angew. Chem., Int. Ed.* **2014**, *53*, 8904−8907.

(13) Moses-DeBusk, M.; Yoon, M.; Allard, L. F.; Mullins, D. R.; Wu, Z.; Yang, X.; Veith, G.; Stocks, G. M.; Narula, C. K. *J. Am. Chem. Soc.* **2013**, *135*, 12634−12645.

(14) Peterson, E. J.; DeLaRiva, A. T.; Lin, S.; Johnson, R. S.; Guo, H.; Miller, J. T.; Kwak, J. H.; Peden, C. H.; Kiefer, B.; Allard, L. F. *Nat. Commun.* **2014**, *5*, 4885.

(15) Liang, J.-X.; Lin, J.; Yang, X.-F.; Wang, A.-Q.; Qiao, B.-T.; Liu, J.; Zhang, T.; Li, J. *J. Phys. Chem. C* **2014**, *118*, 21945−21951.

(16) Lucci, F. R.; Liu, J.; Marcinkowski, M. D.; Yang, M.; Allard, L. F.; Flytzani-Stephanopoulos, M.; Sykes, E. C. H. *Nat. Commun.* **2015**, *6*, 8550.

(17) Qiao, B.; Liu, J.; Wang, Y.-G.; Lin, Q.; Liu, X.; Wang, A.; Li, J.; Zhang, T.; Liu, J. *ACS Catal.* **2015**, *5*, 6249−6254.

(18) Wei, H.; Liu, X.; Wang, A.; Zhang, L.; Qiao, B.; Yang, X.; Huang, Y.; Miao, S.; Liu, J.; Zhang, T. *Nat. Commun.* **2014**, *5*, 5634.

(19) Zhang, S.; Nguyen, L.; Liang, J.-X.; Shan, J.; Liu, J.; Frenkel, A. I.; Patlolla, A.; Huang, W.; Li, J.; Tao, F. *Nat. Commun.* **2015**, *6*, 7938.

(20) Jones, J.; Xiong, H.; DeLaRiva, A. T.; Peterson, E. J.; Pham, H.; Challa, S. R.; Qi, G.; Oh, S.; Wiebenga, M. H.; Hernández, X. I. P. *Science* **2016**, *353*, 150−154.

(21) Liu, W.; Zhang, L.; Yan, W.; Liu, X.; Yang, X.; Miao, S.; Wang, W.; Wang, A.; Zhang, T. *Chem. Sci.* **2016**, *7*, 5758.

(22) Nguyen, L.; Zhang, S.; Wang, L.; Li, Y.; Yoshida, H.; Patlolla, A.; Takeda, S.; Frenkel, A. I.; Tao, F. *ACS Catal.* **2016**, *6*, 840−850.

(23) Wang, L.; Zhang, S.; Zhu, Y.; Patlolla, A.; Shan, J.; Yoshida, H.; Takeda, S.; Frenkel, A. I.; Tao, F. *ACS Catal.* **2013**, *3*, 1011−1019.

(24) Ghosh, T. K.; Nair, N. N. *ChemCatChem* **2013**, *5*, 1811−1821.

(25) Tang, Y.; Wang, Y.-G.; Li, J. *J. Phys. Chem. C* **2017**, *121*, 11281−11289.

(26) Tang, Y.; Zhao, S.; Long, B.; Liu, J.-C.; Li, J. *J. Phys. Chem. C* **2016**, *120*, 17514−17526.

(27) Pingel, T.; Skoglundh, M.; Grönbeck, H.; Olsson, E. *J. Microsc.* **2015**, *260*, 125−132.

(28) Boyes, E. D.; Gai, P. L. *MRS Bull.* **2015**, *40*, 600−609.

(29) Cao, S. W.; Tao, F.; Tang, Y.; Li, Y. T.; Yu, J. G. *Chem. Soc. Rev.* **2016**, *45*, 4747−4765.

(30) Rider, K. B.; Hwang, K. S.; Salmeron, M.; Somorjai, G. A. *J. Am. Chem. Soc.* **2002**, *124*, 5588−5593.

(31) Alayoglu, S.; Somorjai, G. A. *Top. Catal.* **2016**, *59*, 420−438.

(32) Hohenberg, P.; Kohn, W. *Phys. Rev.* **1964**, *136*, B864.

(33) Kohn, W.; Sham, L. J. *Phys. Rev.* **1965**, *140*, A1133.

(34) Chuang, I.-S.; Maciel, G. E. *J. Phys. Chem. B* **1997**, *101*, 3052−3064.

(35) Sindorf, D. W.; Maciel, G. E. *J. Am. Chem. Soc.* **1983**, *105*, 1487−1493.

(36) Wright, A.; Leadbetter, A. *Philos. Mag.* **1975**, *31*, 1391−1401.

(37) Hoffmann, R. *Angew. Chem., Int. Ed.* **2013**, *52*, 93−103.

(38) Handzlik, J.; Ogonowski, J. *J. Phys. Chem. C* **2012**, *116*, 5571−5584.

(39) VandeVondele, J.; Krack, M.; Mohamed, F.; Parrinello, M.; Chassaing, T.; Hutter, J. *Comput. Phys. Commun.* **2005**, *167*, 103−128.

(40) Perdew, J. P.; Burke, K.; Ernzerhof, M. *Phys. Rev. Lett.* **1996**, *77*, 3865.

(41) Lippert, G.; Hutter, J.; Parrinello, M. *Mol. Phys.* **1997**, *92*, 477−488.

(42) VandeVondele, J.; Hutter, J. *J. Chem. Phys.* **2007**, *127*, 114105.

(43) Goedecker, S.; Teter, M.; Hutter, J. *Phys. Rev. B: Condens. Matter Mater. Phys.* **1996**, *54*, 1703.

(44) Henkelman, G.; Jónsson, H. *J. Chem. Phys.* **1999**, *111*, 7010−7022.

(45) Olsen, R.; Kroes, G.; Henkelman, G.; Arnaldsson, A.; Jónsson, H. *J. Chem. Phys.* **2004**, *121*, 9776−9792.

(46) Heyden, A.; Bell, A. T.; Keil, F. J. *J. Chem. Phys.* **2005**, *123*, 224101.

(47) Kästner, J.; Sherwood, P. *J. Chem. Phys.* **2008**, *128*, 014106.

(48) Yang, J. C.; Small, M. W.; Grieshaber, R. V.; Nuzzo, R. G. *Chem. Soc. Rev.* **2012**, *41*, 8179−8194.

(49) *X-Ray Absorption: Principles, Applications, Techniques of EXAFS, SEXAFS and XANES*; Wiley: Hoboken, NJ, 1988.

(50) Tao, F. F.; Shan, J.-j.; Nguyen, L.; Wang, Z.; Zhang, S.; Zhang, L.; Wu, Z.; Huang, W.; Zeng, S.; Hu, P. *Nat. Commun.* **2015**, *6*, 7798.

(51) Jones, J.; Xiong, H. F.; Delariva, A. T.; Peterson, E. J.; Pham, H.; Challa, S. R.; Qi, G. S.; Oh, S.; Wiebenga, M. H.; Hernandez, X. I. P.; Wang, Y.; Datye, A. K. *Science* **2016**, *353*, 150−154.

(52) Almusaiteer, K. A.; Chuang, S. S. *J. Phys. Chem. B* **2000**, *104*, 2265−2272.

(53) Srinivas, G.; Chuang, S. S.; Debnath, S. *J. Catal.* **1994**, *148*, 748−758.

(54) Hecker, W. C.; Bell, A. T. *J. Catal.* **1984**, *85*, 389−397.

(55) Kozuch, S.; Shaik, S. *Acc. Chem. Res.* **2011**, *44*, 101−110.

(56) Xie, H.; Ren, M.; Lei, Q.; Fang, W.; Ying, F. *J. Phys. Chem. C* **2012**, *116*, 7776−7781.

(57) Stull, D. R.; Propher, H. *JANAF Thermochemical Tables*; U.S. National Bureau of Standards: Washington, DC, 1971.

DOI: 10.1021/acscatal.7b01788